BiGlobal linear stability analysis on low-Re flow past an airfoil at high angle of attack

Wei Zhang and Ravi Samtaney

Citation: Phys. Fluids 28, 044105 (2016); doi: 10.1063/1.4945005

View online: http://dx.doi.org/10.1063/1.4945005

View Table of Contents: http://aip.scitation.org/toc/phf/28/4

Published by the American Institute of Physics





BiGlobal linear stability analysis on low-Re flow past an airfoil at high angle of attack

Wei Zhang and Ravi Samtaney

Mechanical Engineering, Physical Sciences and Engineering Division, King Abdullah University of Science and Technology, 4700 KAUST, Thuwal, 23955-6900 Jeddah, Saudi Arabia

(Received 15 June 2015; accepted 5 March 2016; published online 4 April 2016)

We perform BiGlobal linear stability analysis on flow past a NACA0012 airfoil at 16° angle of attack and Reynolds number ranging from 400 to 1000. The steady-state two-dimensional base flows are computed using a well-tested finite difference code in combination with the selective frequency damping method. The base flow is characterized by two asymmetric recirculation bubbles downstream of the airfoil whose streamwise extent and the maximum reverse flow velocity increase with the Reynolds number. The stability analysis of the flow past the airfoil is carried out under very small spanwise wavenumber $\beta = 10^{-4}$ to approximate the two-dimensional perturbation, and medium and large spanwise wavenumbers ($\beta = 1-8$) to account for the three-dimensional perturbation. Numerical results reveal that under small spanwise wavenumber, there are at most two oscillatory unstable modes corresponding to the near wake and far wake instabilities; the growth rate and frequency of the perturbation agree well with the two-dimensional direct numerical simulation results under all Reynolds numbers. For a larger spanwise wavenumber $\beta = 1$, there is only one oscillatory unstable mode associated with the wake instability at Re = 400 and 600, while at Re = 800 and 1000 there are two oscillatory unstable modes for the near wake and far wake instabilities, and one stationary unstable mode for the monotonically growing perturbation within the recirculation bubble via the centrifugal instability mechanism. All the unstable modes are weakened or even suppressed as the spanwise wavenumber further increases, among which the stationary mode persists until $\beta = 4. \odot 2016 AIP Publishing LLC. [http://dx.doi.org/10.1063/1.4945005]$

I. INTRODUCTION

Low Reynolds number flow past an isolated airfoil is relevant to a variety of applications such as micro-air vehicles, insect-type bionic air vehicles, and civil and marine engineering circumstances. Due to an increase in demand from these and related industries, airfoils operating at low-Re regime are needed and are being utilized in engineering applications.¹ The airfoils in these applications are normally operated at high angle of attack (AoA) in order to get sufficient lift, and may consequently suffer from flow separation due to an adverse pressure gradient (APG) field over the suction surface. Flow unsteadiness is commonly encountered in the separated shear layer via the Kelvin-Helmholtz mechanism, and in the wake flow in the form of a Kármán street. The airfoil may experience undesirable load variations as a result of flow unsteadiness which may even induce structural failure. It is clear that flow control in such applications will be an important technological requirement. As a precursor to devising control strategies, we believe it is important to understand and quantify the flow stability characteristics for the low-Re flow past airfoils. Computing the global spectrum of the flow has successfully led to reduced order models (e.g., the work of Berkooz *et al.*² and Schmid³) and control techniques (e.g., the work of Barbagallo *et al.*⁴ and Hervé *et al.*⁵).

Linear stability analysis of the separated flow past an airfoil has been performed based on experimental (e.g., the work of Boutilier and Yarusevych⁶) or direct numerical simulation (DNS) (e.g., the work of Jones *et al.*⁷) result. The time-averaged flow field is usually used as the base flow which is further assumed to be a locally parallel flow. The Orr-Sommerfeld equation⁸ governing



the stability of the viscous parallel flow is then solved to analyze the local stability characteristics in the plane perpendicular to the incoming flow at different streamwise stations. This kind of one-dimensional local stability analysis is suitable for parallel or weakly non-parallel flows in which the flow field only substantially varies in one direction, but is perhaps not an appropriate methodology for the separated flow past an airfoil at high AoA since the flow is essentially non-parallel, especially within the recirculation bubble. The two- or three-dimensionalities of both the base flow and the perturbation have to be taken into account in the stability analysis for a more comprehensive characterization of the flow field and perturbation.

Owing to the growing computing capabilities and the advancements of novel numerical techniques, the three-dimensional global linear stability analysis method, termed as TriGlobal method, is employed for simple non-parallel flows, as reviewed in the works of Theofilis, 9,10 Chomaz, 11 and Sipp et al. 12 The method takes into consideration the three-dimensionality of the base flow and the perturbation, and therefore is the most generalized form of linear stability analysis. However, the generalization is accompanied by the high computational cost which restricts this method in relatively simple geometries (e.g., the work of Tezuka and Suzuki¹³ and Bagheri et al.¹⁴). For most numerical simulations of flow past an isolated airfoil or other configurations using either the high-fidelity DNS or the large-eddy simulation (LES) approach, the computational domain is normally assumed straight in the spanwise direction and periodic boundary condition is prescribed for all primitive variables (e.g., the work of Jones et al., Kitsios et al., Zhang et al., and Zhang and Samtaney 17,18). The variation of the flow along the homogeneous spanwise (z-) direction is significantly weaker than the other two inhomogeneous directions, i.e., $\partial \phi/\partial z \ll \partial \phi/\partial x$ and $\partial \phi/\partial z \ll \partial \phi/\partial y$ in which ϕ is any flow variable. The BiGlobal stability analysis method is proposed to take the advantage of this feature by assuming the perturbation in the form of a normal mode in the spanwise direction, thus the primary perturbation characteristics in the cross-sectional (x-y) plane are preserved and the computational cost is significantly reduced. The BiGlobal linear stability analysis has been employed for a number of physical problems, such as the flow in a channel, ^{19–22} over a backward-facing step^{23–25} or a bluff body.²⁶ It has also been employed for the problem of flow past an isolated airfoil. Theofilis et al.²⁷ first studied the incompressible flow past a NACA0012 airfoil at Re = 1000 and AoA = 5° based on the spectral/hp element method. The results reveal that with a large computational domain, the most unstable mode in the wake is observed far away from the airfoil. More extensive studies have been carried out by Kitsios et al. 15,28 and Rodríguez and Theofilis²⁹ wherein they developed a massively parallel code based on the spectral collocation method and investigated the incompressible flow past a NACA0015 airfoil at Re = 200 and AoA = 18° in which the wake instability is an obvious feature. The results show that the two-dimensional base flow is unstable to the three-dimensional perturbation at spanwise wavenumber $\beta = 1$. The stationary unstable mode corresponding to the instability in the recirculation bubble and the oscillatory unstable mode corresponding to the wake instability are observed under the parameters investigated.

The stability of even higher Reynolds number compressible flow past an airfoil has been analyzed using the two-dimensional global stability analysis approach. 30-33 In these simulations, the Reynolds number is of the order $O(10^5-10^7)$ and the flow is inherently unstable. The first difficulty in performing such a study at a relatively high Reynolds number is the computation of the two-dimensional steady-state base flow. Crouch et al. 30,31 and Iorio et al. 33 solved the steady-state Navier-Stokes equations using the Spalart-Allmaras turbulence model to obtain the base flow, while Fosas de Pando et al. 32 used the time-averaged flow field as the base flow since it is considered to accurately reproduce the frequencies in nonlinear simulations.³⁴ However, the base flow obtained either from the steady Reynolds-Averaged Navier-Stokes (RANS) computation or by time-averaging of the unsteady flow does not necessarily satisfy the steady-state Navier-Stokes equations in principle. The eddy viscosity parameterization in the RANS turbulence model is based on certain assumptions, typically of significance in engineering contexts. Moreover, other assumptions, for example, the balance of turbulent production by dissipation, is confirmed to be invalid for a variety of flow configurations. ^{18,35} Since the near wake flow of a bluff body is accelerated by the flow instability, ³⁶ stability analysis based on the time-averaged flow leads to dramatically different predictions regarding both the growth rate and frequency of the perturbation compared with the stability analysis of a steady-state base flow. 34,37,38



It is concluded from the above discussion that presently the global stability analysis on flow past an isolated airfoil is only performed for low-Re incompressible flow where the base flow can be obtained by directly integrating the governing equations, ^{15,28,29} and for high-Re compressible flow either in the RANS framework or using the time-averaged flow field as the base flow.^{30–33} The objective of the present study is to investigate the stability characteristics of incompressible flow past an airfoil in the low-Re regime Re = 400-1000. The Reynolds number in this study is comparably higher than the previous studies 15,28,29 and the flow is unsteady, thus the results reveal the flow instabilities beyond the first Hopf bifurcation point. The numerical methods employed are free of any assumption or turbulence model, thus both the base flow and the perturbation characteristics are obtained following the original (linearized) Navier-Stokes equations. The base flows are obtained using an in-house finite difference code in combination with the selective frequency damping (SFD) method³⁹ and satisfy the steady-state Navier-Stokes equations. We perform BiGlobal linear stability analysis on the flow past a NACA0012 airfoil at AoA = 16°. Computations are performed for the small spanwise wavenumber to simulate the long-wavelength perturbation which essentially mimic two-dimensional perturbation, and the medium and large spanwise wavenumbers for the small-wavelength perturbation that usually occurs in strong three-dimensional flows. For a detailed understanding of the early development of the perturbation, the present work only focuses on the temporal growth characteristics, while the spatial growth is not covered.

The present work is organized as follows. Section II presents the general descriptions of the physical problem, the mathematical formulation, and the numerical methods. The derivations and assumptions of the governing equations of the perturbation are presented, and the solution method of the generalized eigenvalue equation is presented. Section III presents the results and discussion, including the computation of the base flow and the two-dimensional "DNS" to examine the flow patterns. The stability characteristics of the airfoil separated flow are shown under both small and large spanwise wavenumbers. Some conclusions are given in Section IV. The verification of our code and the summary of the eigenvalue of the unstable modes are given in Appendices A and B.

II. NUMERICAL SETUP

A. Problem description

The schematic configuration of the present simulation is shown in Figure 1 along with the grid details in the region close to the NACA0012 airfoil. The airfoil is rescaled to unit chord length C and is extended to include a sharp trailing edge located at (x/C, y/C) = (1.0, 0.0). The angle of attack is 16°. The physical domain size is 80C in the x-direction with a wake length of 49C, and 60C in the y-direction. This large domain size is chosen based on similar studies by Kitsios et al. 15 and Rodríguez and Theofilis 29 to minimize the effect of the artificially imposed boundary conditions on the flow around the airfoil. The domain is discretized by a 1024×128 C-type grid.

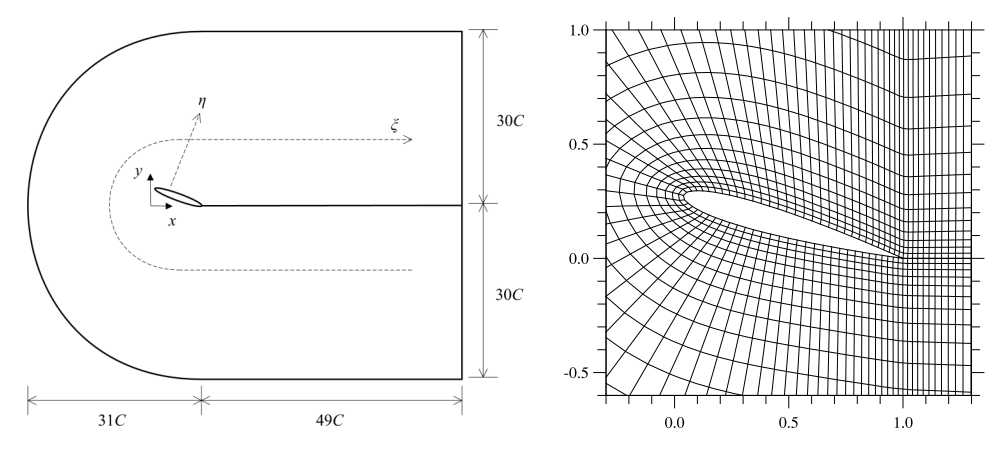


FIG. 1. Schematic of the physical domain and the grid details close to the airfoil. The grid is plotted every fourth gridline in both directions for clarity.



The incompressible flow is coming from the left of the computational domain and leaves from the right side. The velocity of the incoming flow is $(u, v) = (U_0, 0)$. The Reynolds number is defined as $Re = \rho U_0 C/v$, where $\rho = 1$ is the density of the incompressible flow. The stability characteristics of the flow are investigated at Re = 400, 600, 800, and 1000.

B. Governing equations

To determine the stability characteristics of the flow, the primitive variables in the Navier-Stokes equations are expressed as a sum of a steady-state base flow and a perturbation,

$$\phi(x, y, z, t) = \overline{\phi}(x, y) + \varepsilon \phi'(x, y, z, t), \tag{1}$$

where $\phi = (u, v, w, p)$ is the vector of velocity components and pressure, $\overline{\phi}$ is the two-dimensional steady-state base flow, and $\varepsilon \phi'$ ($\ll \overline{\phi}$) is the perturbation. For the BiGlobal linear stability analysis, the perturbed velocity and pressure are assumed in the form,

$$\phi'(x, y, z, t) = \hat{\phi}(x, y)e^{i\beta z + \lambda t} + \text{c.c. (complex conjugate)},$$
 (2)

where z is the spanwise direction, t is the time, β is the spanwise wavenumber (here we restrict $\beta \in R$), and $\lambda = \text{Re}(\lambda) + i \text{Im}(\lambda)$ is the complex circular frequency in which the real part $\text{Re}(\lambda)$ is the growth/damping rate and the imaginary part $\text{Im}(\lambda)$ is the phase angle. Since the perturbation is physically a real number, it is customary to add the complex conjugate. A positive $\text{Re}(\lambda)$ indicates the exponential growth of the unstable mode, while a negative value reflects the damping of the perturbation in time. The flow is considered unstable if it has at least one eigenmode with positive $\text{Re}(\lambda)$.

In BiGlobal stability analysis, we consider three-dimensional perturbation on a two-dimensional steady-state base flow. Since the flow is assumed homogeneous in the spanwise direction, the perturbations are either stationary or traveling in opposite z-direction. Consequently, the expression of the perturbation in Eq. (2) can be simplified without loss of generality by considering only the symmetric Fourier modes as 23,24,40,41

$$u'(x, y, z, t) = \hat{u}(x, y)\cos(\beta z)e^{\lambda t} + \text{c.c.},$$
(3)

$$v'(x, y, z, t) = \hat{v}(x, y)\cos(\beta z)e^{\lambda t} + \text{c.c.},$$
(4)

$$w'(x, y, z, t) = \hat{w}(x, y)\sin(\beta z)e^{\lambda t} + \text{c.c.},$$
(5)

$$p'(x, y, z, t) = \hat{p}(x, y)\cos(\beta z)e^{\lambda t} + \text{c.c.}$$
(6)

This simplification reduces the storage requirement for our BiGlobal analysis compared with the original formulation since all the coefficients in the eigenvalue equation are real, as shown below.

Recall that the base flow is steady-state and two-dimensional and the primitive variables in Eq. (1) are substituted into the original Navier-Stokes equations with the following assumptions:

$$\overline{w} = 0, \qquad \overline{\phi}_z = 0, \qquad \overline{\phi}_t = 0,$$
 (7)

in which the subscript indicates the spatial or temporal differentiation. The resulting equations for the base flow are

$$\overline{u}_x + \overline{v}_u = 0, \tag{8}$$

$$\overline{u}\,\overline{u}_x + \overline{v}\,\overline{u}_y = -\overline{p}_x/\rho + (\overline{u}_{xx} + \overline{u}_{yy})/\text{Re},\tag{9}$$

$$\overline{u}\,\overline{v}_x + \overline{v}\,\overline{v}_y = -\overline{p}_y/\rho + (\overline{v}_{xx} + \overline{v}_{yy})/\text{Re}.\tag{10}$$

The linearized equations for the perturbations by omitting the high-order infinitesimal terms become

$$\hat{u}_x + \hat{v}_u + \beta \hat{w} = 0, \tag{11}$$

$$\lambda \hat{u} + \overline{u}\hat{u}_x + \overline{v}\hat{u}_u + \hat{u}\overline{u}_x + \hat{v}\overline{u}_u = -\hat{p}_x/\rho + (\hat{u}_{xx} + \hat{u}_{uu} - \beta^2\hat{u})/\text{Re},\tag{12}$$

$$\lambda \hat{v} + \overline{u}\hat{v}_x + \overline{v}\hat{v}_y + \hat{u}\overline{v}_x + \hat{v}\overline{v}_y = -\hat{p}_y/\rho + (\hat{v}_{xx} + \hat{v}_{yy} - \beta^2\hat{v})/\text{Re}, \tag{13}$$

$$\lambda \hat{w} + \overline{u}\hat{w}_x + \overline{v}\hat{w}_y = \beta \hat{p}/\rho + (\hat{w}_{xx} + \hat{w}_{yy} - \beta^2 \hat{w})/\text{Re}. \tag{14}$$

The computation of the base flow solution will be discussed in Section III B. Governing Equations (11)-(14) for the perturbations are spatially discretized by the second-order central



difference scheme. Zero boundary condition is prescribed for the perturbed velocity at the airfoil surface and the inflow boundary, and homogeneous Neumann condition at the outflow boundary. The pressure satisfies the compatibility condition at the airfoil surface and is extrapolated at the far field boundaries. ^{15,40}

C. Solution method

The governing equations for the perturbations (Eqs. (11)-(14)) can be cast as a generalized eigenvalue problem,

$$A\hat{\phi} = \lambda M\hat{\phi},\tag{15}$$

where the eigenvalue λ , the eigenfunction $\hat{\phi} = (\hat{u}, \hat{v}, \hat{w}, \hat{\rho})$, and the spatial discretization operator A are functions of the mesh and the parameter space $(\overline{\phi}, \text{Re}, \beta)$. In this study, this system is solved for the eigenpair $(\lambda, \hat{\phi})$ using the implicitly restarted Arnoldi method (IRAM) in the ARPACK package. Since it is practically expensive to obtain all the eigenmodes, we only search for all the unstable eigenmodes (Re(λ) > 0) and a portion of the least-stable ones. The shift-invert transformation is employed to accelerate the convergence. Given a complex shift σ , Eq. (15) is transformed as

$$(A - \sigma M)^{-1} M \hat{\phi} = \hat{\phi} / (\lambda - \sigma). \tag{16}$$

The ARPACK package is used to solve Eq. (16) to find a certain number of eigenvalues closest to the complex shift σ . Since the IRAM works in a reverse communication mode, we have to repeatedly provide the vector $(A - \sigma M)^{-1}M\hat{\phi}$ to the solver. Instead of the expensive inversion operation on the large sparse matrix $(A - \sigma M)^{-1}$, we assume $V = (A - \sigma M)^{-1}M\hat{\phi}$ ($V \in C$) and compute V by solving the following linear system:

$$(A - \sigma M)V = M\hat{\phi}. \tag{17}$$

The linear system is solved using the MUMPS package^{43,44} which utilizes the multifrontal LU factorization. The coefficient matrix $A - \sigma M$ is factorized and stored in the initialization stage, and Eq. (17) is repeatedly solved during the solution procedure to provide the solution vector V to the ARPACK solver. We choose a number of complex shift σ to cover a sufficiently large region of Re(λ) > 0 in the complex plane in search for the unstable eigenmodes, and the least-stable ones by choosing a number of complex shifts with Re(σ) = 0 and 0 < Im(σ) < 10. Since the operator A is real, it has complex conjugate eigenvalues that are symmetric about the real axis, hence we only search for those with Im(σ) \geqslant 0. Note that the conjugate ones are not plotted in the following figures. To ensure the convergence and correctness of the computed eigenmodes, we use the following criterion for both the real and imaginary parts of the eigenpairs to keep only the converged results:³²

$$||A\hat{\phi} - \lambda M\hat{\phi}||_{\infty} < 10^{-6}, \qquad ||(A\hat{\phi} - \lambda M\hat{\phi})/(A\hat{\phi})||_{2} < 10^{-3}.$$
 (18)

The code for the BiGlobal linear stability analysis is verified through the problem of Poiseuille flow in a duct, as described in Appendix A.

III. RESULTS AND DISCUSSION

A. Two-dimensional unsteady flow

We first perform nonlinear two-dimensional "DNS" (this is not DNS in the strictest sense as this flow is not 3D) on the unsteady flow around the airfoil under different Reynolds numbers for a general understanding of the flow pattern. A 1024×128 grid is employed as shown in Figure 1, and the same mesh in the x-y plane is also used for the BiGlobal stability analysis. These 2D results are obtained using a semi-implicit fractional step finite difference method. The momentum equations are spatially discretized by a second-order central difference scheme, and temporally discretized by the Adams-Bashforth scheme for the convective terms and implicit scheme for the viscous terms. Uniform incoming flow is prescribed at the inlet and convective condition is applied at the outflow boundary. The simulation starts from a zero field and is integrated in time for about



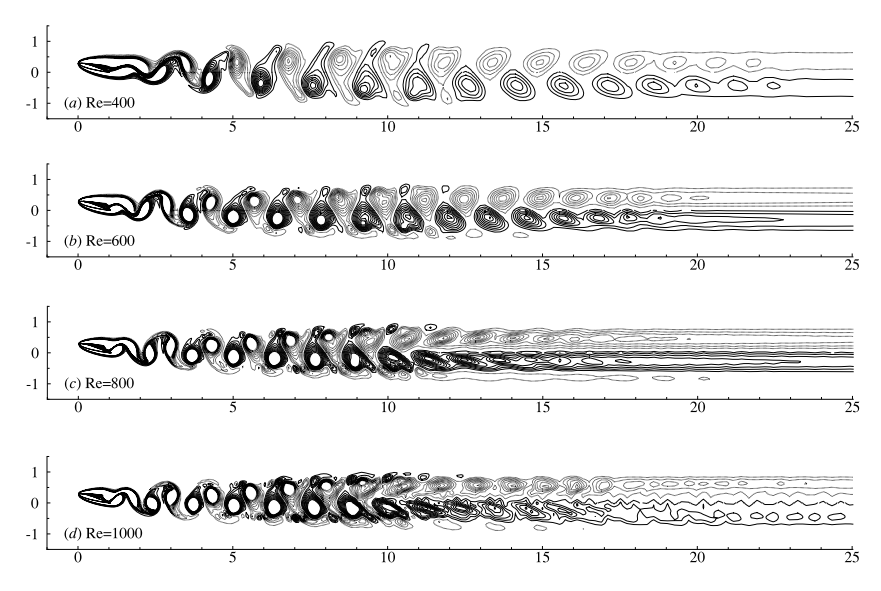


FIG. 2. Instantaneous vorticity field for the two-dimensional unsteady simulation plotted at $\omega = [-2, 2]$ with $\Delta \omega = 0.1$.

 $200C/U_0$. For the Reynolds numbers under investigation, the grid is guaranteed to be sufficiently fine around the airfoil with normalized mesh spacings of $\Delta \xi_{\rm max}^+ \approx 2.7$ and $\Delta \eta_{\rm max}^+ \approx 1.4$ for the first layer grid. These normalized mesh spacings are well within the limits imposed by well accepted mesh spacing criterion for turbulent simulations⁴⁵ and the mesh is deemed sufficient for the present study. The simulations are performed using an in-house code that has been validated in our previous works. ^{16–18}

The unsteady flow pattern is presented by the instantaneous vorticity field in Figure 2. The periodic shedding of the flow is clearly observed downstream of the airfoil. The low-Re flow is well organized and behaves with perfect time periodicity. As the Reynolds number increases, the flow becomes less periodic and more stochastic especially in the far wake region. The different wake patterns are further quantified by the temporal power spectra of velocity monitored at some certain probes as shown in Figure 3. The probes are placed to record the time histories of the transverse velocity v/U_0 above the middle of the airfoil (P1), above the trailing edge (P2), and in the near and far wake regions (P3-P5). The Strouhal number slightly increases with the Reynolds number. The flow is time-periodic upstream of the trailing edge and in the near wake (P1-P4) for all Reynolds numbers, as seen by the sharp fundamental and its integer multiple harmonics. For Re \geq 600, the spectrum of the transverse velocity in the far wake (P5) tends to become broadband without clear harmonics and the fundamental frequency slightly shifts, reflecting the growing non-periodic fluctuations. The loss of perfect time periodicity in the far wake region is observed for Re = 1000 in Figure 2.

B. Base flow

The base flow is the equilibrium state about which the stability characteristics are investigated. The flow past an airfoil becomes unsteady when the Reynolds number is beyond some critical value depending on the airfoil geometry and angle of attack. The base flow normally cannot be obtained by directly integrating the Navier-Stokes equations in time since the unstable nature of the flow will induce vortex shedding making the flow unsteady, never attaining a steady state. The base flow solution can be computed by directly solving the nonlinear boundary value problem written in Eqs. (8)-(10) using the Newton-type methods, but this requires a specific solver. In order to efficiently compute the base flow by slightly revising an existing Navier-Stokes solver, Åkervik *et al.*³⁹ proposed the SFD method to obtain the steady solution of the Navier-Stokes equations. In this method, a forcing term and a time derivative term are added to the momentum equation,



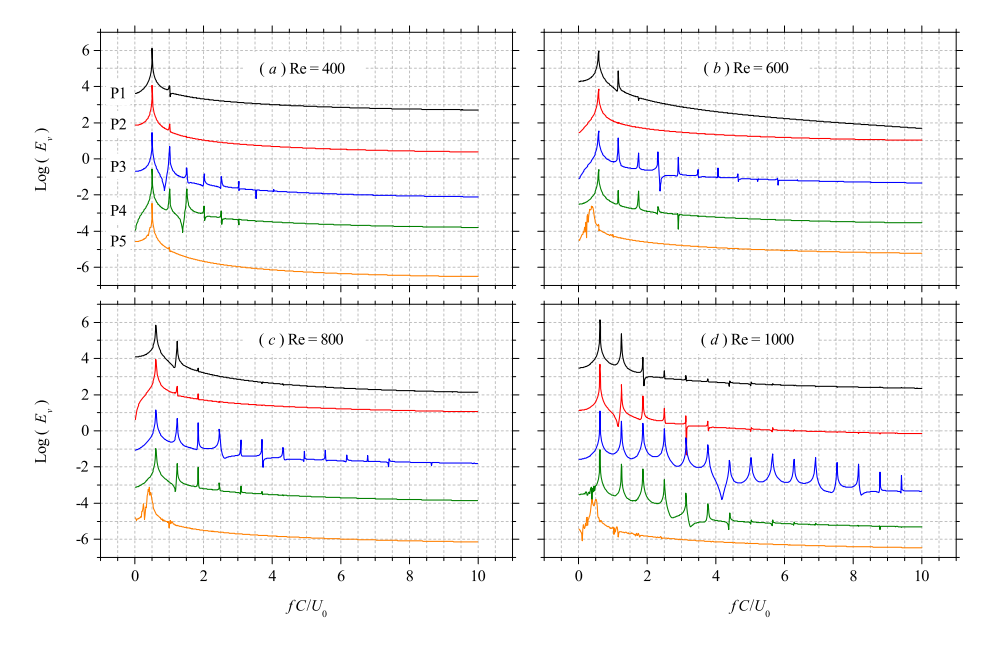


FIG. 3. Temporal power spectra of the transverse velocity v/U_0 measured by probes at different positions. The coordinates of the probes are (from P1 to P5): (x/C, y/C) = (0.5776, 0.3037), (0.9965, 0.4179), (1.4975, 0.0028), (4.9823, 0.0044), and (20.0787, -0.0113). The spectra in each subfigure are artificially separated for clarity.

$$\overline{\mathbf{u}}_t + (\overline{\mathbf{u}} \cdot \nabla)\overline{\mathbf{u}} = -\nabla \overline{p}/\rho + \nabla^2 \overline{\mathbf{u}}/\text{Re} - \chi(\overline{\mathbf{u}} - \mathbf{q}), \tag{19}$$

where $\overline{\mathbf{u}}$ is the velocity vector of the base flow and \mathbf{q} is a field vector with the same unit as $\overline{\mathbf{u}}$; χ is a positive user-defined parameter. An extra ordinary differential equation (ODE) is also added to the system of governing equations,

$$\mathbf{q}_t = (\overline{\mathbf{u}} - \mathbf{q})/\Delta,\tag{20}$$

where Δ is also a positive user-defined parameter. The additions of the forcing term and time derivative term and the ODE provide a feedback mechanism to the original governing equations to damp the unstable modes. By solving the system of equations with proper values of χ and Δ (respectively, 1.0 and 5.0 in this work), the steady base flow is obtained satisfying $\overline{\mathbf{u}}_t \simeq 0$ and $\mathbf{q} \simeq \overline{\mathbf{u}}$ after the computation converges.

In the present study the governing equations for the base flow are solved by integrating in time using a semi-implicit fractional step method. The derivatives are spatially discretized by the second-order central difference scheme with a cell-centered formulation. Figure 4 shows the convergence histories of the maximum values of $|\overline{\mathbf{u}} - \mathbf{q}|$ for the streamwise and transverse velocity components. In all of our computations, the maximum pointwise residual typically converges to $O(10^{-13})$,

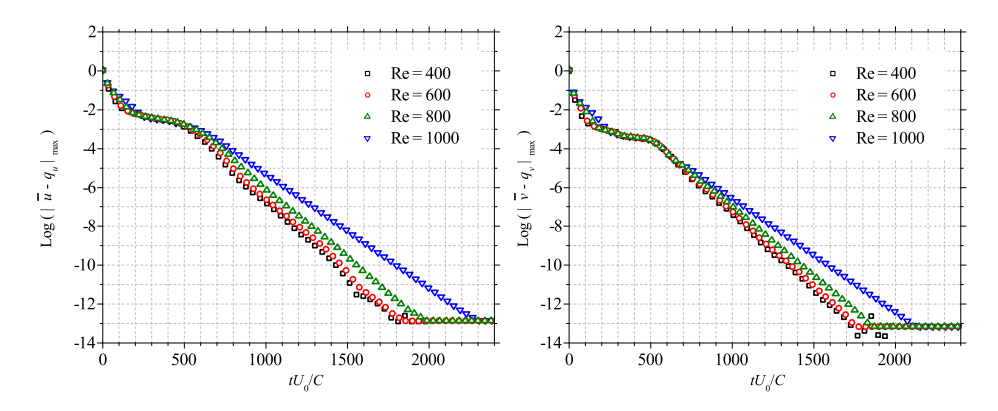


FIG. 4. Convergence histories of $|\overline{\mathbf{u}} - \mathbf{q}|_{\text{max}}$ for the computation of the base flow.



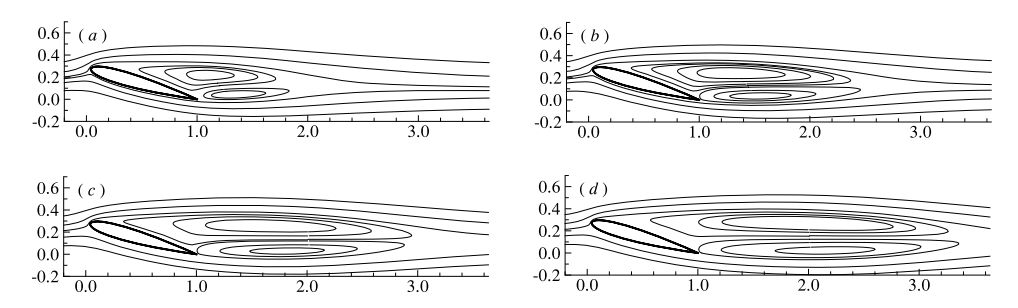


FIG. 5. Streamlines of the base flows for (from (a) to (d)) Re = 400, 600, 800 and 1000.

which guarantees a steady-state (possibly unstable) base flow solution satisfying Eqs. (8)-(10). The base flow solution and its spatial derivatives are then substituted into Eqs. (11)-(14) for the computations of the eigenpair $(\lambda, \hat{\phi})$.

The base flows obtained by the SFD method at different Reynolds numbers are presented in Figure 5. The streamlines are plotted around the airfoil and in the near wake. The flow topology is quite similar for all Reynolds numbers. Two asymmetric counter-rotating recirculation bubbles form above the leeward surface and downstream of the trailing edge. The two bubbles are of different sizes due to the inclination of the airfoil with the upper bubble being the larger one. As the Reynolds number increases, the size of the two bubbles noticeably increases in the streamwise direction with a minor increase in the transverse direction. The bubbles are unstable and periodic shedding will commence in the unsteady Navier-Stokes simulation after the constraints (the forcing term and ODE) are removed. Figure 6 shows the distribution of the negative streamwise velocity, representing the reverse flow in the recirculation bubbles. As the Reynolds number increases, the reverse flow becomes dominant in the near wake; it covers a larger area extending downstream with monotonically increasing maximum velocity. The variation of the streamwise velocity profile in the wake is shown in Figure 7. Consistent with the findings in Figure 6, the velocity deficiency is more pronounced as the Reynolds number increases and gets weaker away from the airfoil, although still discernible in the far wake x/C = 30. The nonuniform distribution of the streamwise velocity along the y-direction reflects the non-zero strain, and there is an inflection point in the velocity profile in both the near wake and far wake. The two-dimensional base flow may be invisciblly unstable based on the Rayleigh criteria.8

C. BiGlobal stability analysis for small spanwise wavenumber

In this section, the BiGlobal linear stability analysis is performed for a small spanwise wavenumber $\beta = 10^{-4}$. The steady flows shown in Figure 5 serve as the base flows. For the small wavenumber, the spanwise wavelength of the perturbation is sufficiently large $(L = 2\pi/\beta)$ that the stability characteristics ought to be close to flow subjected solely to two-dimensional perturbation $(\beta = 0)$. Figure 8 shows the unstable and a portion of the least-stable eigenvalues. It is noted here that the stable modes are discrete as predicted by the present modal analysis; however, they will not be further analyzed

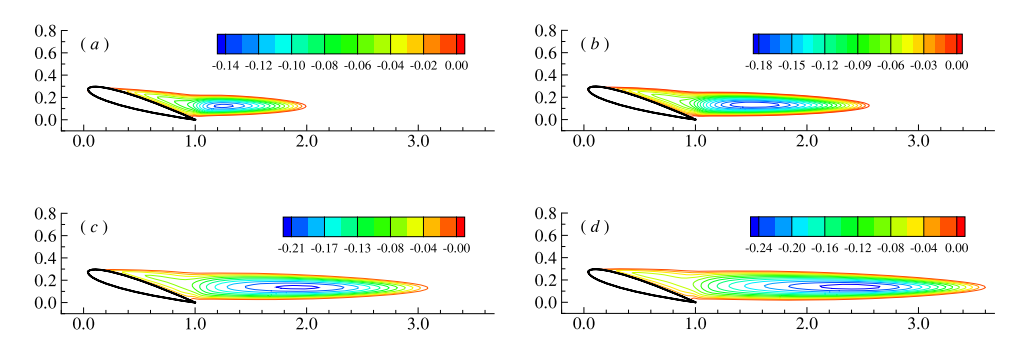


FIG. 6. Streamwise velocity \overline{u}/U_0 of the recirculating flow for (from (a) to (d)) Re = 400, 600, 800 and 1000.



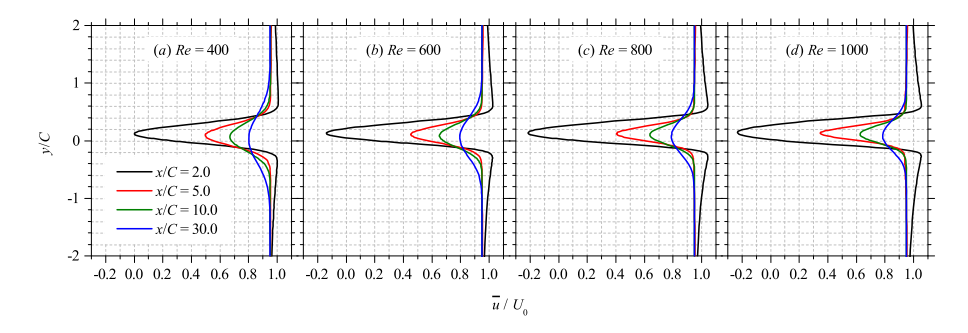


FIG. 7. Streamwise velocity distributions in the wake for the base flow.

since we are only interested in the unstable modes. The flow is unstable to the three-dimensional perturbation under all Reynolds numbers investigated as eigenvalues with positive real part are observed. The perturbations with lower frequency are amplified or weakly damped, while the high frequency ones are strongly damped. There is one distinct oscillatory unstable mode with non-zero $\text{Im}(\lambda)$ at Re = 400 and 600, while two are observed at Re = 800 and 1000, namely, the primary and secondary oscillatory modes, with the former one has a larger $\text{Re}(\lambda)$. The secondary oscillatory mode corresponds to the far wake instability and is also observed in the two-dimensional global stability analysis for flow past a circular cylinder when the Reynolds number beyonds a critical value. As the Reynolds number increases, the flow becomes more unstable as the growth rate of the primary oscillatory mode increases and the stable modes are less damped. There appears a branch of weakly unstable modes with medium frequencies as shown in the inset of the figure, which is also observed in the works of Kitsios *et al.* 15 and Rodríguez and Theofilis. These weakly unstable modes correspond to the far wake instability biased towards to the outflow boundary which makes the flow less regularized compared with the time-periodic state in the near wake region (see the curve of P5 in Figure 3) and are possibly caused by the truncation of the computational domain. 47

To examine the dependency on mesh resolution, a similar analysis with the same domain size $(80C \times 60C)$ but a finer 2048×256 mesh is carried out at Re = 1000. The computed results, in terms of the growth rate and frequency of the primary oscillatory mode, are close to those obtained with the present 1024×128 mesh with a maximum relative error of about 2.8%. To limit the computational expenditure, we continue all further computations with the present 1024×128 mesh.

The spatial structure of the primary oscillatory mode is shown in Figure 9 by the real part of the streamwise and transverse perturbed velocities scaled by $|\hat{w}|_{max}$ (and the same hereafter). The structures exhibit classical features of the wake type mode that are expected in flow past bluff bodies. The perturbation originates in the near wake where the separated shear layer starts to shed. As the Reynolds number increases, the perturbed flow is more dominant in the near wake but is less pronounced in the downstream region. The Reynolds number has a decisive effect on the perturbed velocities in that both $Re(\hat{u})$ and $Re(\hat{v})$ increase in magnitude with it, reflecting the progressively dominant two-dimensional perturbed flow field at high Reynolds numbers.

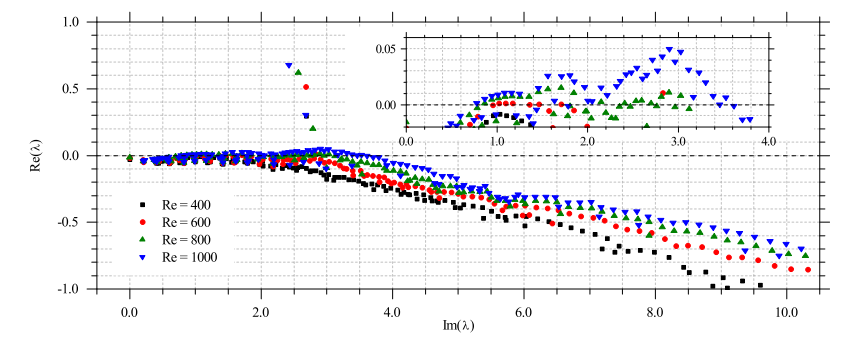


FIG. 8. Eigenvalue spectra at $\beta = 10^{-4}$.



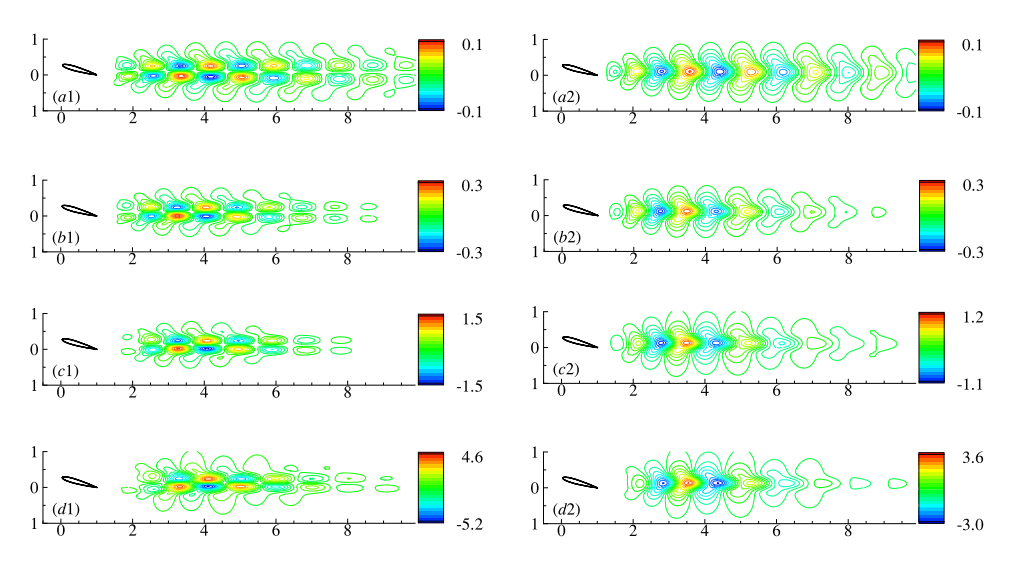


FIG. 9. Eigenfunctions of Re(\hat{u}) (left column) and Re(\hat{v}) (right column) of the primary oscillatory mode at $\beta = 10^{-4}$: (a) Re = 400 and $\lambda = (0.2956, 2.6921)$; (b) Re = 600 and $\lambda = (0.5126, 2.6794)$; (c) Re = 800 and $\lambda = (0.6202, 2.5664)$; (d) Re = 1000 and $\lambda = (0.6783, 2.4254)$.

Since the BiGlobal linear stability analysis at $\beta = 10^{-4}$ is partly aimed at examining the stability characteristics of the two-dimensional flow, we separately perform two-dimensional "DNS" to compare the early stage of the temporal growth of the perturbation. The continuity equation and Eq. (19) (without the forcing term) are directly integrated in time using our solver described in Section III A, and the perturbed velocity is recorded at several probes downstream of the airfoil trailing edge. Three direct simulations are carried out with different initial conditions. The first is the BF case in which the direct simulation is initialized with the base flow solution $(\overline{u}, \overline{v}, \overline{p})$; the infinitesimal perturbation then originates from the round-off error and numerical residual. The second case is termed as BF+P14; the initial condition is taken as the base flow solution $(\overline{u}, \overline{v}, \overline{p})$ superimposed with the perturbation (u', v', p') obtained from the primary oscillatory mode of the BiGlobal stability analysis, as exemplified in Figure 9; the perturbation is scaled with the maximum magnitude $\sqrt{u'^2 + v'^2}$ equals to 10^{-14} . In this case, the perturbation stems from both the round-off error and numerical residual as well as the artificially imposed initial perturbation. The third case is termed as BF+P10, which is similar to the previous one except that the maximum magnitude equals to 10^{-10} . The temporal growth of the perturbed transverse velocity is given in Figure 10. The maximum perturbed velocity grows exponentially (i.e., linearly when plotted using the natural logarithmic scale), and the growth rate increases with the Reynolds number. The three simulations give

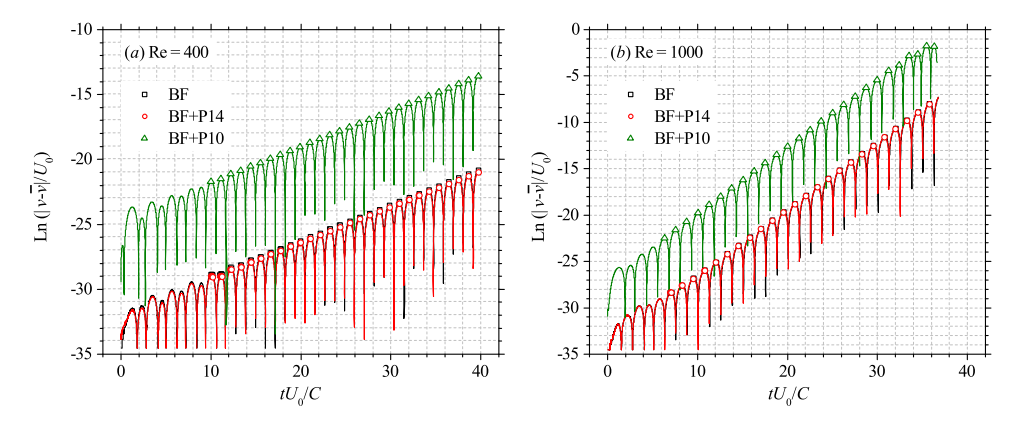


FIG. 10. Temporal growth of the perturbed transverse velocity $|v - \overline{v}|/U_0$ probed at (x/C, y/C) = (1.4975, 0.0028) for the three 2D "DNS" studies. The hollow symbols indicate the local maximum value.



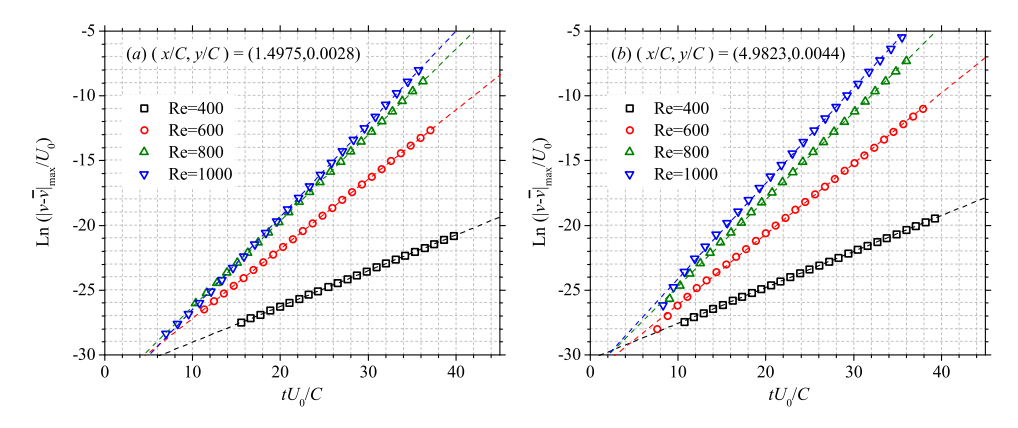


FIG. 11. Temporal growth of the local maximum value of $|v - \overline{v}|/U_0$.

consistent predictions regarding the growth rate and frequency. It is noted that the BF and BF+P14 cases produce almost identical growth histories, while the perturbed velocity in the BF+P10 case is several orders of magnitude larger. By comparing the results in the three cases, we can safely conclude that the combination of round-off error and numerical residual is sufficiently reliable and effective in stimulating perturbations and reproducing its temporal development within the linear regime.

The time history of the local maximum perturbation of the BF case is extracted and plotted in Figure 11 for the evaluation of the growth rate and frequency of the perturbation. The local maximum of the perturbed velocity during the very initial stage $(t \to 0)$ is not shown because its small magnitude value ($<10^{-13}$) prevents an accurate quantification. The growth rate and frequency are estimated from the slope and the horizontal interval of the discrete maxima, respectively, during the exponential growth stage in Figures 10 and 11. The perturbed transverse velocity recorded at the two probes show identical growth rate and frequency at all Reynolds numbers, hence we only list the results obtained from the near wake probe (x/C, y/C) = (1.4975, 0.0028) in Table I since it corresponds to the primary oscillatory (most unstable) mode. It is seen in the table that the BiGlobal stability analysis yields good predictions in terms of the growth rate and frequency of the perturbation at all Reynolds numbers, which justifies the assumption that the stability analysis at small spanwise wavenumber reflects the growth of the nominally two-dimensional perturbation. We, therefore, consider the reliability of the present BiGlobal stability analysis code to be properly validated.

D. BiGlobal stability analysis for medium and large spanwise wavenumbers

In this section, the BiGlobal linear stability analysis is performed for medium and large spanwise wavenumbers at $\beta = 1, 2, 4$, and 8 to study the stability characteristics of the two-dimensional base flow to three-dimensional perturbation. For each successive wavenumber, the spanwise wavelength is halved. Figure 12 gives the eigenvalue spectra at $\beta = 1$. The spectra are generally similar

TABLE I. Summary of the growth rate and frequency of the perturbation predicted by the 2D "DNS" and the BiGlobal linear stability analysis at $\beta = 10^{-4}$. The first value in each cell is the growth rate and the second is the frequency. For the 2D "DNS", the two values are estimated from Figure 11(a). For the BiGlobal linear stability analysis, the two values are calculated from the eigenvalue of the primary oscillatory mode in Figure 8, in which the growth rate is $\text{Re}(\lambda)$ and the frequency is $\text{Im}(\lambda)/2\pi$.

Item	Re = 400	600	800	1000
2D "DNS"	(0.2754, 0.4549)	(0.5363, 0.4459)	(0.6625, 0.4247)	(0.7160, 0.3994)
BiGlobal analysis	(0.2956, 0.4285)	(0.5126, 0.4264)	(0.6202, 0.4085)	(0.6783, 0.3860)
Relative difference (%)	(7.3, 5.8)	(4.4, 4.4)	(6.4, 3.8)	(5.3, 3.4)



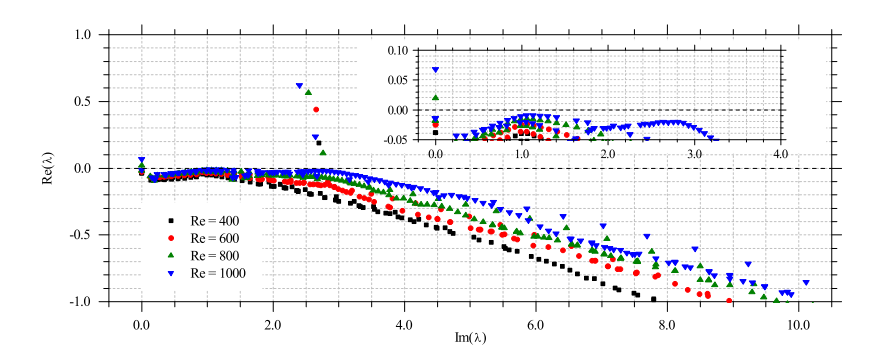


FIG. 12. Eigenvalue spectra at $\beta = 1$.

to those obtained at $\beta = 10^{-4}$ in that there is one oscillatory mode for Re = 400 and 600 but two for Re = 800 and 1000. The weakly unstable modes associated to the far wake instability observed at $\beta = 10^{-4}$ are suppressed. We observe a stationary mode with $\text{Im}(\lambda) = 0$ at Re = 800 and 1000, which implies that the perturbation grows exponentially in time without phase angle variation. The modal structures of the oscillatory mode for Re = 400 are shown in Figure 13 by the real parts of the perturbed velocity and pressure. The oscillatory mode corresponds to the wake instability and is two-dimensionally dominated with $Re(\hat{u}) > Re(\hat{w})$ and $Re(\hat{v}) > Re(\hat{w})$. The perturbed velocity and pressure exhibit similar structures at Re = 600 as shown in Figure 14, which are only pronounced within a small region in the near wake close to the airfoil but are negligible for x/C > 12. Both the maximum values of $Re(\hat{u})$ and $Re(\hat{v})$ increase in magnitude, showing stronger perturbations in the x-y plane. The modal structures of the three unstable modes for Re = 1000, namely, the primary oscillatory, secondary oscillatory and stationary modes, are shown in Figures 15-17. The secondary oscillatory mode appearing at the relatively higher Reynolds numbers is attributed to the far wake instability. The eigenfunctions show similar spatial structures as the primary oscillatory mode with more significant in-plane perturbation. The stationary mode is relevant to the growth of perturbation in the recirculation bubbles and is much weaker than the two oscillatory modes.

The existence of the stationary mode relevant to the recirculation bubble is dependent on the flow configuration and other parameters. Such a mode is also observed by Kitsios *et al.*¹⁵ for an ellipse and a NACA0015 airfoil at Re = 200 and β = 1. The underlying instability mechanism is complicated and has been discussed in many studies. In contrast to the Kelvin-Helmholtz mechanism, Theofilis *et al.*⁵⁰ discovered the existence of the self-excited three-dimensional instability

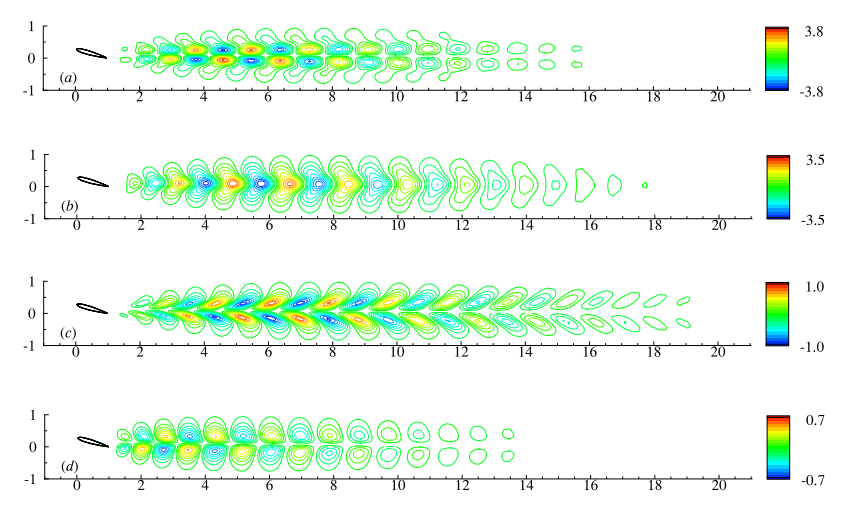


FIG. 13. Eigenfunctions of the primary oscillatory mode $\lambda = (0.1877, 2.6927)$ at Re = 400 and $\beta = 1$: (a) Re(\hat{u}); (b) Re(\hat{v}); (c) Re(\hat{u}); (d) Re(\hat{p}).



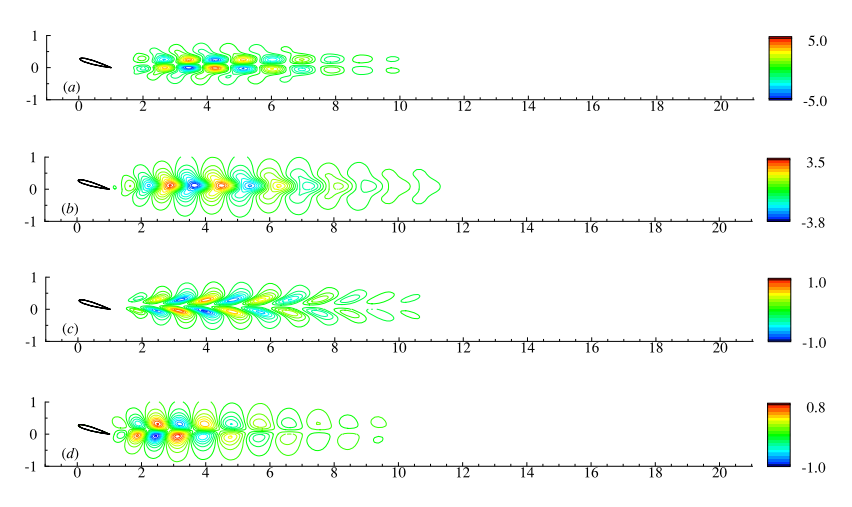


FIG. 14. Eigenfunctions of the primary oscillatory mode $\lambda = (0.4396, 2.6543)$ at Re = 600 and $\beta = 1$: (a) Re(\hat{u}); (b) Re(\hat{v}); (c) Re(\hat{w}); (d) Re(\hat{p}).

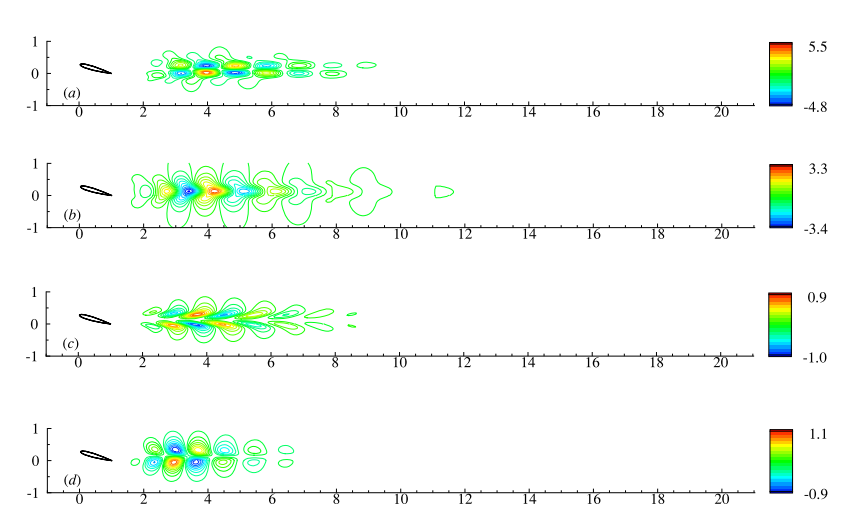


FIG. 15. Eigenfunctions of the primary oscillatory mode $\lambda = (0.6239, 2.4013)$ at Re = 1000 and $\beta = 1$: (a) Re(\hat{u}); (b) Re(\hat{v}); (c) Re(\hat{w}); (d) Re(\hat{p}).

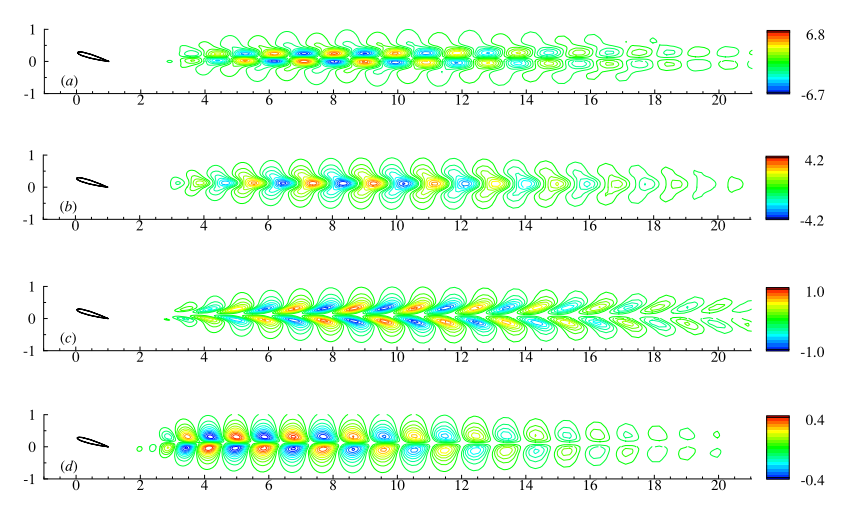


FIG. 16. Eigenfunctions of the secondary oscillatory mode $\lambda = (0.2393, 2.6479)$ at Re = 1000 and $\beta = 1$: (a) $Re(\hat{u})$; (b) $Re(\hat{v})$; (c) $Re(\hat{w})$; (d) $Re(\hat{p})$.



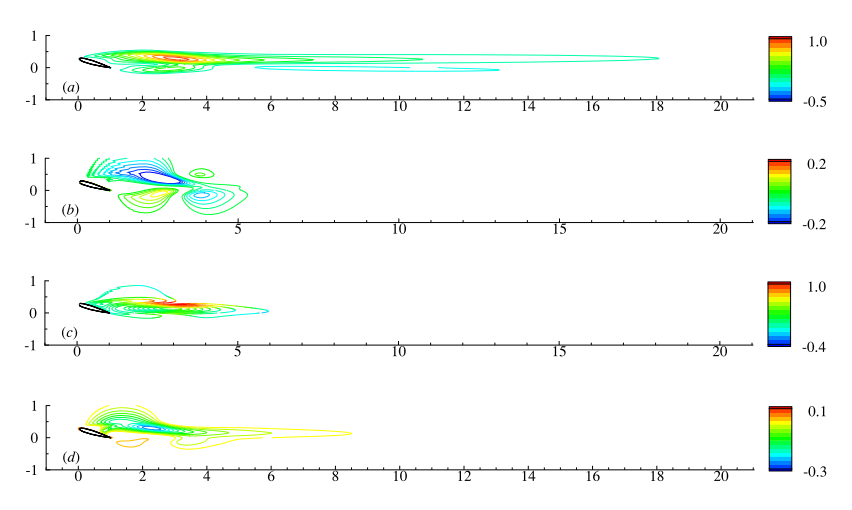


FIG. 17. Eigenfunctions of the stationary mode $\lambda = (0.0683, 0.0000)$ at Re = 1000 and $\beta = 1$: (a) Re(\hat{u}); (b) Re(\hat{v}); (c) Re(\hat{w}); (d) Re(\hat{p}).

mode in the laminar separation bubble (LSB) formed on a flat plate. The structure of the LSB was later examined by Rodríguez and Theofilis.⁵¹ The recirculation bubble may possibly act as an amplifier for environment disturbances, or as an oscillator to sustain the instability waves propagated into it.⁵² For the present airfoil at a high angle of attack, it is shown in Figures 5 and 6 that the recirculation bubbles elongate in the streamwise direction so that the base flow induces significant strain in the wake. The recirculating flow is distinctly different from the LSB on the flat plate which is spatially restricted within a small region. The stationary mode is resulted from the centrifugal instability through which the nominally two-dimensional recirculating flow is unstable to three-dimensional perturbation and results in a discrete unstable eigenmode, as observed in a number of different geometries with a two-dimensional recirculation bubble. 15,23,53 The centrifugal instability is found to emerge with sufficiently strong reverse flow. For the LSB on a flat plate, Alam and Sandham⁵⁴ concluded, from examining three-dimensional DNS, that a maximum reverse flow velocity $u_{rev}/U_0 = 8\%$ leads to the onset of unsteadiness. A similar value of 7% is found by Rodríguez et al.⁵⁵ where the effect of the Reynolds number is limited. For the present flow configuration, the recirculating wake flow is free of the bounded wall, and the stationary mode stemming from the centrifugal instability is only observed at Re = 800 and 1000 where $u_{rev}/U_0 > \approx 20\%$ at the spanwise wavenumber $\beta = 1$, as shown in Figure 6.

The effect of the spanwise wavenumber on the stability characteristics at Re = 1000 is shown in Figure 18: there are three unstable modes at $\beta = 1$ and 2. As the wavenumber increases, the oscillatory modes first diminish and then the stationary mode is suppressed, resulting in one stationary mode at $\beta = 4$ and no unstable mode at $\beta = 8$. The spatial structures of the eigenfunction Re(\hat{a}) at $\beta = 2$ and $\beta = 4$ are, respectively, shown in Figures 19 and 20. The eigenfunctions of various unstable modes have similar spatial structure as those of $\beta = 1$, while their magnitude decreases

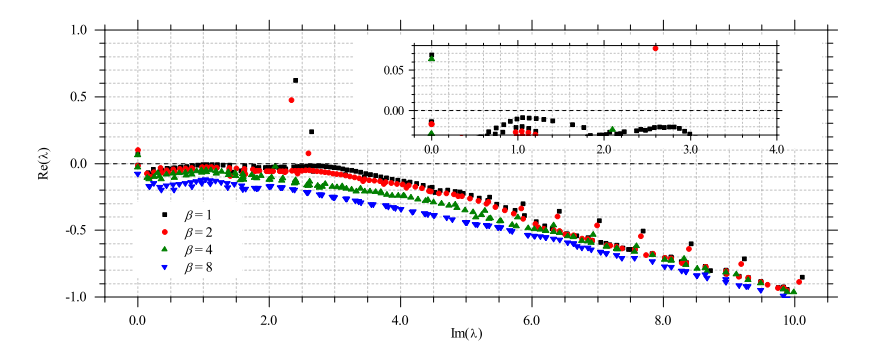


FIG. 18. Eigenvalue spectra at Re = 1000.



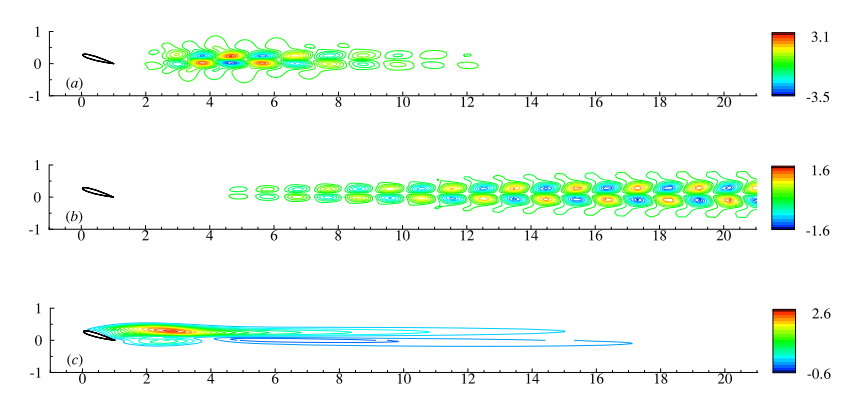


FIG. 19. Eigenfunction of Re(\hat{u}) at Re = 1000 and β = 2: (a) primary oscillatory mode λ = (0.4739, 2.3392); (b) secondary oscillatory mode λ = (0.0767, 2.5955); (c) stationary mode λ = (0.1000, 0.0000).

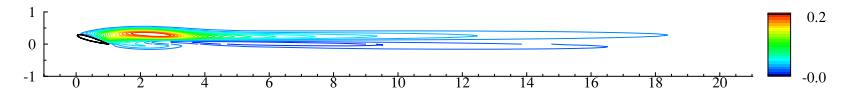


FIG. 20. Eigenfunction of Re(\hat{u}) at Re = 1000 and β = 4 for the stationary mode λ = (0.0633, 0.0000).

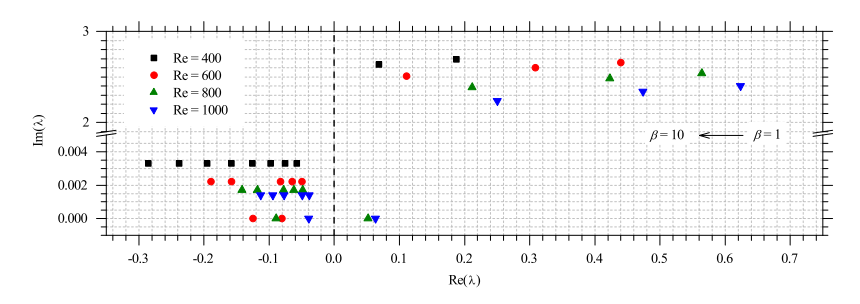


FIG. 21. The effect of the spanwise wavenumber on the eigenvalue of the most-unstable/least-stable mode. The spanwise wavenumber is $\beta = 1-10$ with $\Delta\beta = 1$.

with the wavenumber. A minor difference observed for the secondary oscillatory mode at $\beta = 2$ is that the perturbation is only significant in the very far wake region.

The variation of the most-unstable/least-stable eigenvalue with respect to the spanwise wavenumber is shown in Figure 21. A complete summary for the variations of various unstable modes with the spanwise wavenumber and Reynolds number is given in Appendix B. One consistent conclusion drawn is that the growth rate of the most-unstable mode decreases with the spanwise wavenumber and eventually transitions to stable beyond a critical value. The critical value is computed approximately using the bisection technique based on the criterion that neutral stability is reached when the real part of the most-unstable/least-stable eigenvalue is zero. We continue the bisection iterations until $|\text{Re}(\lambda)|$ is smaller than 0.01. The critical spanwise wavenumbers are approximately 2.42, 3.47, 4.29 and 4.42 for the Reynolds number 400, 600, 800, and 1000, respectively. The neutral-stable mode is quasi-stationary with negligibly small $Im(\lambda)$.

IV. CONCLUSION

We perform BiGlobal linear stability analysis on flow past a NACA0012 airfoil at 16° angle of attack and Reynolds number from 400 to 1000. The stability analysis is conducted under the small spanwise wavenumber $\beta = 10^{-4}$ for the approximation of two-dimensional perturbation with long spanwise wavelength, and medium and large spanwise wavenumbers for the three-dimensional perturbation with short spanwise wavelength. The two-dimensional steady base flows are computed by our finite difference solver using the selective frequency damping method. The base flow comprises of two asymmetric recirculation bubbles downstream of the airfoil, and their sizes in the



streamwise direction and the maximum reverse flow velocity notably grow with the Reynolds number.

At the small spanwise wavenumber, there are strong oscillatory unstable modes at all Reynolds numbers investigated. There is one oscillatory mode for Re = 400 and 600 which is associated to the wake instability. At Re = 800 and 1000, two oscillatory modes appear with nearly the same frequency, i.e., the primary oscillatory mode with larger growth rate for the near wake instability, and the secondary oscillatory mode for the far wake instability. The perturbations in the cross-sectional plane (\hat{u}, \hat{v}) dominate the spanwise component as the Reynolds number increases, reflecting a significant two-dimensionally growing pattern. In order to assess the validity of the two-dimensional approximation at the present small spanwise wavenumber, direct simulations are carried out initialized by the base flow, with or without the superimposed perturbation from the primary oscillatory mode. The direct simulation well reproduces the exponential growth of the perturbation at all Reynolds numbers. The growth rate and frequency of the primary oscillatory (most unstable) mode predicted by the direct simulation and BiGlobal stability analysis are consistent with each other, which validates the code and the two-dimensional approximation.

For the medium spanwise wavenumber $\beta=1$, there is one oscillatory wake mode for Re = 400 and 600 and two for Re = 800 and 1000, similarly to the $\beta=10^{-4}$ case. The wake mode is two-dimensionally dominated. As the Reynolds number increases, the domination is more pronounced, and the eigenfunctions representing the perturbation are getting to be significant within a smaller region close to the airfoil. A stationary mode is observed for Re = 800 and 1000 corresponding to the monotonically growing perturbation without phase angle variation (Re(λ) > 0 and Im(λ) = 0). The stationary mode appears as a result of the centrifugal instability of the recirculation bubble as long as the reverse flow is strong enough at higher Reynolds numbers, which is about $u_{rev}/U_0 = 20\%$ for the present flow configuration where u_{rev} is the maximum reverse flow velocity. Both the oscillatory and stationary modes are suppressed as the spanwise wavenumber increases; the oscillatory mode first diminishes while the stationary mode still exists till $\beta=4$. The critical spanwise wavenumbers for the stabilization of the flow at different Reynolds number are also presented.

ACKNOWLEDGMENTS

The work was supported by the KAUST Office of Competitive Research Funds under Award No. URF/1/1394-01. The IBM Blue Gene/P Shaheen at KAUST was utilized for the simulations.

APPENDIX A: CODE VERIFICATION VIA POISEUILLE FLOW IN A DUCT

The numerical method and code are verified through the duct Poiseuille flow problem. Considering a rectangular duct defined in the domain $(x, y) \in [-A, A] \times [-1, 1]$ with A the aspect ratio, the fluid is moving in the z-direction driven by the constant streamwise pressure gradient. The base flow is independent of the z-coordinate and possesses a vector $(0, 0, \overline{w})$. The \overline{w} -velocity satisfies a Poisson equation derived by simplifying the Navier-Stokes equations and has a two-dimensional parabolic profile as a series solution, ⁵⁶

$$\overline{w}(x,y) = 1 - y^2 - 4\left(\frac{2}{\pi}\right)^3 \sum_{n=0}^{\infty} \frac{(-1)^n}{(2n+1)^3} \frac{\cosh[(2n+1)\pi x/2]\cos[(2n+1)\pi y/2]}{\cosh[(2n+1)\pi A/2]}.$$
 (A1)

The velocity vector $(0,0,\overline{w})$ computed from Eq. (A1) serves as the base flow solution. The Reynolds number is defined based on the half-duct depth and the \overline{w} -velocity at the center of the duct (the maximum value). In this case, the base flow is varying in the x-y plane but is uniform for the base flow and periodic for the perturbations in the streamwise (z-) direction. The governing equations for the perturbations are thus different from Eqs. (11)-(14) and are written as follows:

$$\hat{u}_x + \hat{v}_u + i\beta\hat{w} = 0, (A2)$$

$$\lambda \hat{u} + i\beta \overline{w}\hat{u} = -\hat{p}_x/\rho + (\hat{u}_{xx} + \hat{u}_{yy} - \beta^2 \hat{u})/\text{Re},\tag{A3}$$

$$\lambda \hat{v} + i\beta \overline{w}\hat{v} = -\hat{p}_{u}/\rho + (\hat{v}_{xx} + \hat{v}_{uu} - \beta^{2}\hat{v})/\text{Re}, \tag{A4}$$



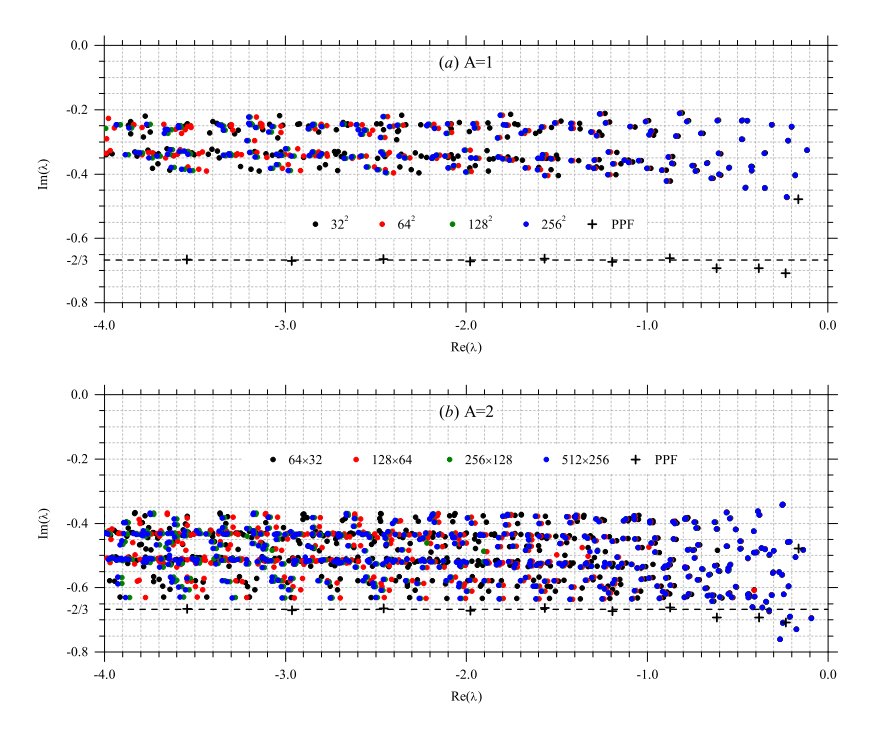


FIG. 22. Eigenvalue spectra of the least-stable modes of the duct Poiseuille flow obtained under various resolutions at Re = 100 and $\beta = 1$.

$$\lambda \hat{w} + i\beta \overline{w}\hat{w} + \hat{u}\overline{w}_x + \hat{v}\overline{w}_y = -i\beta \hat{p}/\rho + (\hat{w}_{xx} + \hat{w}_{yy} - \beta^2 \hat{w})/\text{Re}. \tag{A5}$$

We perform the BiGlobal stability analysis on this duct Poiseuille flow with parameters Re = 100, $\beta = 1$, and A = 1 and 2 to be consistent with the works by Theofilis et al.⁴⁰ and Merzari et al.²¹ A uniform mesh is used for this verification, with the spatial resolution ranging from 32² to 256² for the square duct (A = 1), and from 64×32 to 512×256 for the rectangular one (A = 2). The eigenvalue spectra for the plane Poiseuille flow (PPF) at Re = 100 is computed by solving the Orr-Sommerfeld equation corresponding to the extreme case $A \to \infty$. The eigenvalue spectra computed under various resolutions are shown in Figure 22. At the present Reynolds number and spanwise wavenumber, the flow is stable to three-dimensional perturbations and all eigenvalues lie to the left of the imaginary axis. The distributions of the eigenvalues are in agreement with those obtained by Theofilis et al. 40 who utilized a Legendre collocation method on a 64×32 grid. For both ducts of different aspect ratios, the low resolution mesh is not capable to reproduce the grid-independent result towards the most-stable regime $(Re(\lambda) \to -\infty)$ in that the eigenvalues are generally shifting along the real axis. As the resolution increases, the scattering gradually reduces so that the computed eigenvalues overlap in the eye-norm, and these results are in good agreement with those in Theofilis et al.⁴⁰ It is also noted here that the least-stable eigenvalues ($Re(\lambda) \rightarrow 0$) are well predicted under various grid resolutions, and it is precisely that these modes, together with the unstable modes, are important and interested in our work. As the aspect ratio increases from A = 1 to A = 2, the eigenvalues of the stable modes move towards the P-branch of the PPF case at $Im(\lambda) = -2/3$. For higher Reynolds numbers and/or larger aspect ratios, it is computationally expensive to reproduce even part of the stable eigenvalue spectrum since a large mesh has to be employed to properly capture the velocity gradient in the thinning boundary layer. Based on the above result, we believe that the present numerical method and code are reliable for the stability analysis of flow past an airfoil.

APPENDIX B: EFFECT OF REYNOLDS NUMBER AND SPANWISE WAVENUMBER ON THE UNSTABLE MODES

Table II lists the variation of the eigenvalue of the three possible unstable modes (primary oscillatory, secondary oscillatory and stationary) with the Reynolds number and spanwise wavenumber.



TABLE II. Variations of the growth rate and frequency of the unstable modes $(Re(\lambda), Im(\lambda))$ with the Reynolds number and spanwise wavenumber.

β	Re = 400	600	800	1000					
	Primary oscillatory mode								
1	(0.1877, 2.6927)	(0.4396, 2.6543)	(0.5644, 2.5403)	(0.6239, 2.4013)					
2	(0.0682, 2.6372)	(0.3086, 2.5979)	(0.4231, 2.4814)	(0.4739, 2.3392)					
3		(0.1109, 2.5066)	(0.2116, 2.3843)	(0.2503, 2.2368)					
	Secondary oscillatory mode								
1			(0.1124, 2.7639)	(0.2393, 2.6479)					
2				(0.0767, 2.5955)					
	Stationary mode								
1			(0.0191, 0.0000)	(0.0683, 0.0000)					
2			(0.0745, 0.0000)	(0.1000, 0.0000)					
3			(0.0725, 0.0000)	(0.0876, 0.0000)					
4			(0.0523, 0.0000)	(0.0633, 0.0000)					

We searched for the unstable modes up to $\beta = 10$, while the results for the stable modes are not presented. All unstable modes are generally weakened with the decrease of Reynolds number or increase of spanwise wavenumber. The secondary oscillatory and stationary modes are totally suppressed at Re = 400 and 600.

²¹ E. Merzari, S. Wang, H. Ninokata, and V. Theofilis, "Biglobal linear stability analysis for the flow in eccentric annular channels and a related geometry," Phys. Fluids 20, 114104 (2008).



¹ D. J. Pines and F. Bohorquez, "Challenges facing future micro-air-vehicle development," J. Aircr. 43, 290–305 (2006).

² G. Berkooz, P. Holmes, and J. L. Lumley, "The proper orthogonal decomposition in the analysis of turbulent flows," Annu. Rev. Fluid Mech. **25**, 539–575 (1993).

³ P. J. Schmid, "Dynamic mode decomposition of numerical and experimental data," J. Fluid Mech. 656, 5–28 (2010).

⁴ A. Barbagallo, D. Sipp, and P. J. Schmid, "Closed-loop control of an open cavity flow using reduced-order models," J. Fluid Mech. 641, 1–50 (2009).

⁵ A. Hervé, D. Sipp, P. J. Schmid, and M. Samuelides, "A physics-based approach to flow control using system identification," J. Fluid Mech. 702, 26–58 (2012).

⁶ M. S. H. Boutilier and S. Yarusevych, "Separated shear layer transition over an airfoil at a low Reynolds number," Phys. Fluids **24**, 084105 (2012).

⁷ L. E. Jones, R. D. Sandberg, and N. D. Sandham, "Direct numerical simulations of forced and unforced separation bubbles on an airfoil at incidence," J. Fluid Mech. 602, 175–207 (2008).

⁸ P. G. Drazin and W. M. Reid, *Hydrodynamic Stability* (Cambridge University Press, 2004).

⁹ V. Theofilis, "Advances in global linear instability analysis of nonparallel and three-dimensional flows," Prog. Aerosp. Sci. 39, 249–315 (2003).

¹⁰ V. Theofilis, "Global linear instability," Annu. Rev. Fluid Mech. 43, 319–352 (2011).

¹¹ J.-M. Chomaz, "Global instabilities in spatially developing flows: Non-normality and nonlinearity," Annu. Rev. Fluid Mech. **37**, 357–392 (2005).

¹² D. Sipp, O. Marquet, P. Meliga, and A. Barbagallo, "Dynamics and control of global instabilities in open-flows: A linearized approach," Appl. Mech. Rev. 63, 030801 (2010).

¹³ A. Tezuka and K. Suzuki, "Three-dimensional global linear stability analysis of flow around a spheroid," AIAA J. 44, 1697–1708 (2006).

 ¹⁴ S. Bagheri, P. Schlatter, P. J. Schmid, and D. S. Henningson, "Global stability of a jet in crossflow," J. Fluid Mech. 624, 33–44 (2009).

¹⁵ V. Kitsios, D. Rodríguez, V. Theofilis, A. Ooi, and J. Soria, "Biglobal stability analysis in curvilinear coordinates of massively separated lifting bodies," J. Comput. Phys. 228, 7181–7196 (2009).

¹⁶ W. Zhang, W. Cheng, W. Gao, A. Qamar, and R. Samtaney, "Geometrical effects on the airfoil flow separation and transition," Comput. Fluids 116, 60–73 (2015).

¹⁷ W. Zhang and R. Samtaney, "A direct numerical simulation investigation of the synthetic jet frequency effects on separation control of low-Re flow past an airfoil," Phys. Fluids 27, 055101 (2015).

¹⁸ W. Zhang and R. Samtaney, "Assessment of spanwise domain size effect on the transitional flow past an airfoil," Comput. Fluids 124, 39–53 (2016).

¹⁹ R. E. Pitt, S. J. Sherwin, and V. Theofilis, "Biglobal stability analysis of steady flow in constricted channel geometries," Int. J. Numer. Methods Fluids 47, 1229–1235 (2005).

²⁰ S. V. Malik and A. P. Hooper, "Three-dimensional disturbances in channel flows," Phys. Fluids 19, 052102 (2007).

- ²² J. M. Floryan and M. Asai, "On the transition between distributed and isolated surface roughness and its effect on the stability of channel flow," Phys. Fluids 23, 104101 (2011).
- ²³ D. Barkley, M. G. M. Gomes, and R. D. Henderson, "Three-dimensional instability in flow over a backward-facing step," J. Fluid Mech. 473, 167–190 (2002).
- ²⁴ H. M. Blackburn, D. Barkley, and S. J. Sherwin, "Convective instability and transient growth in flow over a backward-facing step," J. Fluid Mech. 603, 271–304 (2008).
- ²⁵ D. Lanzerstorfer and H. C. Kuhlmann, "Global stability of the two-dimensional flow over a backward-facing step," J. Fluid Mech. 693, 1–27 (2012).
- ²⁶ L. M. González, V. Theofilis, and R. Gómez-Blanco, "Finite element methods for viscous incompressible biglobal instability analysis on unstructured meshes," AIAA J. 45, 840–854 (2007).
- ²⁷ V. Theofilis, D. Barkley, and S. Sherwin, "Spectral/hp element technology for global flow instability and control," Aeronaut. J. 106, 619–625 (2002).
- ²⁸ V. Kitsios, D. Rodríguez, V. Theofilis, A. Ooi, and J. Soria, "Biglobal instability analysis of turbulent flow over an airfoil at an angle of attack," AIAA Paper 2008-4384 (2008).
- ²⁹ D. Rodríguez and V. Theofilis, "Massively parallel solution of the biglobal eigenvalue problem using dense linear algebra," AIAA J. 47, 2449–2459 (2009).
- ³⁰ J. D. Crouch, A. Garbaruk, and D. Magidov, "Predicting the onset of flow unsteadiness based on global instability," J. Comput. Phys. 224, 924–940 (2007).
- ³¹ J. D. Crouch, A. Garbaruk, D. Magidov, and A. Travin, "Origin of transonic buffet on aerofoils," J. Fluid Mech. 628, 357–369 (2009)
- ³² M. Fosas de Pando, P. J. Schmid, and D. Sipp, "A global analysis of tonal noise in flows around aerofoils," J. Fluid Mech. 754, 5–38 (2014).
- ³³ M. C. Iorio, L. M. González, and E. Ferrer, "Direct and adjoint global stability analysis of turbulent transonic flows over a NACA0012 profile," Int. J. Numer. Methods Fluids 76, 147–168 (2014).
- ³⁴ D. Barkley, "Linear analysis of the cylinder wake mean flow," Europhys. Lett. **75**, 750–756 (2006).
- ³⁵ H. Le, P. Moin, and J. Kim, "Direct numerical simulation of turbulent flow over a backward-facing step," J. Fluid Mech. 330, 349–374 (1997).
- ³⁶ B. J. A. Zielinska, S. Goujon-Durand, J. Dušek, and J. E. Wesfreid, "Strongly nonlinear effect in unstable wakes," Phys. Rev. Lett. 79, 3893–3896 (1997).
- ³⁷ D. Sipp and A. Lebedev, "Global stability of base and mean flows: A general approach and its applications to cylinder and open cavity flows," J. Fluid Mech. 593, 333–358 (2007).
- ³⁸ S. Mittal, "Global linear stability analysis of time-averaged flows," Int. J. Numer. Methods Fluids 58, 111–118 (2008).
- ³⁹ E. Åkervik, L. Brandt, D. S. Henningson, J. Hæpffner, O. Marxen, and P. Schlatter, "Steady solutions of the Navier-Stokes equations by selective frequency damping," Phys. Fluids 18, 068102 (2006).
- ⁴⁰ V. Theofilis, P. W. Duck, and J. Owen, "Viscous linear stability analysis of rectangular duct and cavity flows," J. Fluid Mech. 505, 249–286 (2004).
- ⁴¹ A. Frédéric, R. Jean-Christophe, and G. Xavier, "A domain decomposition matrix-free method for global linear stability," Comput. Fluids 66, 63–84 (2012).
- ⁴² R. B. Lehoucq, D. C. Sorensen, and C. Yang, ARPACK Users' Guide: Solution of Large-Scale Eigenvalue Problems with Implicitly Restarted Arnoldi Methods (SIAM, 1998).
- ⁴³ P. R. Amestoy, I. S. Duff, J. Y. L'Excellent, and J. Koster, "A fully asynchronous multifrontal solver using distributed dynamic scheduling," SIAM J. Matrix Anal. Appl. 23, 15–41 (2001).
- ⁴⁴ P. R. Amestoy, A. Guermouche, J. Y. L'Excellent, and S. Pralet, "Hybrid scheduling for the parallel solution of linear systems," Parallel Comput. 32, 136–156 (2006).
- ⁴⁵ N. J. Georgiadis, D. P. Rizzetta, and C. Fureby, "Large-eddy simulation: Current capabilities, recommended practices, and future research," AIAA J. 48, 1772–1784 (2010).
- ⁴⁶ A. Verma and S. Mittal, "A new unstable mode in the wake of a circular cylinder," Phys. Fluids 23, 121701 (2011).
- ⁴⁷ D. Rodríguez, "Global instability of laminar separation bubbles," Ph.D. thesis, Technical University of Madrid, 2010.
- ⁴⁸ O. Marquet, D. Sipp, and L. Jacquin, "Sensitivity analysis and passive control of cylinder flow," J. Fluid Mech. 615, 221–252 (2008).
- ⁴⁹ N. Abdessemed, S. J. Sherwin, and V. Theofilis, "Linear instability analysis of low-pressure turbine flows," J. Fluid Mech. 628, 57–83 (2009).
- ⁵⁰ V. Theofilis, S. Hein, and U. Dallmann, "On the origins of unsteadiness and three-dimensionality in a laminar separation bubble," Philos. Trans. R. Soc., A 358, 3229–3246 (2000).
- ⁵¹ D. Rodríguez and V. Theofilis, "Structural changes of laminar separation bubbles induced by global linear instability," J. Fluid Mech. 655, 280–305 (2010).
- ⁵² P. Huerre and P. A. Monkewitz, "Local and global instabilities in spatially developing flows," Annu. Rev. Fluid Mech. 22, 473–537 (1990).
- ⁵³ F. Gallaire, M. Marquillie, and U. Ehrenstein, "Three-dimensional transverse instabilities in detached boundary layers," J. Fluid Mech. 571, 221–233 (2007).
- ⁵⁴ M. Alam and N. D. Sandham, "Direct numerical simulation of 'short' laminar separation bubbles with turbulent reattachment," J. Fluid Mech. 403, 223–250 (2000).
- ⁵⁵ D. Rodríguez, E. M. Gennaro, and M. P. Juniper, "The two classes of primary modal instability in laminar separation bubbles," J. Fluid Mech. 734, R4 (2013).
- ⁵⁶ L. Rosenhead, *Laminar Boundary Layers* (Oxford Clarendon Press, 1963).

